Supplementary Information to "Spatial and Temporal Distribution of Ocean Iron Fertilization and CO_2 drawdown during the Last Glacial Termination"

Fabrice Lambert, Pontifical Catholic University of Chile, Santiago Chile
5   Natalia Opazo, Pontifical Catholic University of Chile, Santiago Chile
Andy Ridgwell, University of California, Riverside, USA
Gisela Winckler, LDEO, Columbia University, New York, USA
Frank Lamy, Alfred Wegener Institute, Bremerhaven, Germany
Gary Shaffer, University of Magallanes, Punta Arenas, Chile
10 Karen Kohfeld, Simon Fraser University, Burnaby, Canada
Rumi Ohgaito, Japan Agency for Marine-Earth Science and Technology, Yokohama, Japan
Samuel Albani, University of Milano-Bicocca, Milano, Italy
Ayako Abe-Ouchi, University of Tokyo, Tokyo, Japan

15 Corresponding Author: F. Lambert (lambert@uc.cl)

cGENIE Model Simulations

In this paper we employed the current "muffin" version of the cGenie Earth System Model of Intermediate Complexity (EMIC), which is hosted on GitHub at https://github.com/derpycode/cgenie.muffin (with a corresponding user manual detailing installation, configuration, and tutorials available from https://github.com/derpycode/muffindoc).

The physical/climatological configuration of cGenie we employ is the same as that of Cao et al. (2009), and generates a present-day ocean circulation reasonably consistent with the observed large-scale patterns (and particularly, regional inventories) of radiocarbon, anthropogenic CO_2, and CFC11 (see Cao et al. (2009) for details). The representation of marine (and ocean-atmosphere) carbon cycling is similar to Cao et al. (2009), except for the addition of iron co-limitation of biological productivity at the surface together with basic sources (dust) and sinks (non-reversible scavenging) of dissolved Fe in the ocean. This Fe-enabled ocean carbon cycle scheme is the same as used by Tagliabue et al. (2016) in a recent marine iron cycle model inter-comparison study, and is described and evaluated in more detail as follows.

For iron supply to the ocean, we assume here just a single source – dust, and create 6 different late Holocene and LGM gridded dust climatologies to force the model with (as described elsewhere). Although the observed iron fraction within dust can range from 1-9 wt% depending on dust mineralogy and provenance (Fung et al., 2000), we follow previous modelling studies (e.g. (Doney et al., 2006; Parekh et al., 2005, 2004; Tagliabue et al., 2009)), and set the iron fraction to the mean crustal abundance value of 3.5 wt%. To convert the solid iron flux delivered to the ocean surface, to a flux of dissolved iron that becomes bioavailable to phytoplankton, we take into account observations of solubility being inversely related to the suspended particle concentration (Baker et al., 2006), and set:

$$r_{Fesol} = \gamma_{Fesol} \cdot (C_{dust})^{-0.5} \qquad\qquad\qquad\qquad \text{(Eq. S1)}$$

40   where r_{Fesol} is the fractional solubility of Fe in dust, γ_{Fesol} is a scaling factor, and C_{dust} is the concentration of dust in the surface ocean layer (mol kg^{-1}) – calculated as the input of dust to a surface ocean grid point in the model that occurs within a single time-step, divided by the seawater mass of the grid cell. The value of γ_{Fesol} is applied spatially, and continuously re-calculated in the model in order to achieve a specific mean flux-weighted average solubility – $\bar{r}_{Fesol}$. We set: $\bar{r}_{Fesol} = 0.29\%$

45   following a number of recent applications of the cGENIE iron cycle model (e.g. (Ödalen et al., 2020; Tagliabue et al., 2016)). Importantly, the inverse relationship leads to a very substantial model-generated heterogeneity in apparent iron solubility – from as low as 0.047% in the Mediterranean (and under the highest dust fluxes), to almost 7% in the Southern Ocean (associated with the lowest dust fluxes to the ocean surface anywhere).

50   The inverse relationship between dust flux and iron solubility leads to a reduction in the heterogeneity in dissolved iron flux to the ocean surface, as compare to the applied dust flux field. Figure S1 shows the solid iron flux fields for each of the 6 (late Holocene) dust reconstructions tested in this paper, plus the preindustrial iron field of Mahowald et al. (2006) which was used as the iron forcing to cGENIE in the Tagliabue et al. (2016) model inter-comparison study ('FeMIP'). In Figure S2 we show the

55   corresponding fields of dissolved Fe flux to the ocean surface that result from the application of the inverse relationship embodied in Eq. S1. Both sets of figures are plotted using a 3 order-of-magnitude scale in order to highlight the reduced spatial heterogeneity (and inter dust reconstructions differences) in dissolved Fe flux as compared to the driving dust flux (Figure 3, main text).

The corresponding (to each of the 6 dust reconstructions, plus the preindustrial dust field of Mahowald

60   et al. (2006)) distributions of dissolved iron at the ocean surface, compared to observations of dissolved iron concentrations, are shown in Figure S3. The observations are from Tagliabue et al.

(2016) and are re-gridded to the cGENIE ocean grid before plotting. Differences are most pronounced in the South Atlantic, North Pacific, and the Indian Ocean, with the Lambert reconstruction providing a visually better fit to observations in the South Atlantic, FeMIP and Lambert providing the better

65 apparent fits in the North Pacific, and FeMIP, Lambert, and MRI-CGCM3 providing visually better agreement in the Indian Ocean, as compared to the other dust reconstructions. The consequences for the ocean carbon cycle as a whole are illustrated in Figure S4, which shows the difference between mean annual ocean surface phosphate concentrations in cGENIE, minus the climatological (observationally based) field (Garcia et al., 2018).

70 For the loss terms of dissolved iron from the ocean in cGENIE – iron is taken up along with phosphate and carbon during biological productivity at the ocean surface, with the Fe:C ratio being a function of ambient dissolved Fe concentrations (Ridgwell, 2001), with higher Fe:C (C/Fe) ratios under conditions of iron limitation, and lower Fe:C (lower C/Fe and hence higher intercellular iron quotas) when bioavailable Fe is freely available. In seawater, dissolved iron in the model exists in either 'free' or

75 ligand-bound form, with an equilibrium partitioning between them following Parekh et al. (2005). Non ligand-bound dissolved iron is subject to scavenging onto sinking particulate organic matter (POM) and removal from the water column, again following Parekh et al. (2005). Loss of iron from the ocean and the balance to input from dust at the surface, is through the fluxes of: (i) Fe incorporated in POM, and (ii) Fe scavenged onto POM, that reach the sediment surface. At the ocean floor, while organic

80 matter is assumed fully remineralized with its constituents returned in dissolved form back to the ocean (a reflective boundary condition – (Hülse et al., 2018), all associated Fe, whether originally intercellular, or scavenged, is assumed lost (and at steady state balances surface input).

Parameters in the model setting the mean global (flux-weighted) iron solubility in dust, and the scaling for the rate of dissolved Fe scavenging onto sinking POM, were roughly calibrated against a previous

‘open-ocean’ observational dataset of distributions of dissolved iron concentrations in the ocean ((Moore and Braucher, 2008)). These parameter values were used in the Tagliabue et al. (2016) study, and we employ them without any re-calibration here.

The configuration of cGENIE we used here, albeit driven with the pre-industrial dust field of Mahowald et al. (2006) (and not one of the 6 alternative Holocene/LGM dust reconstruction pairs we test here), was previously assessed as part of an ocean iron cycle model inter-comparison project. This involved a total of 13 models, differing in e.g. the resolution at which ocean circulation was calculated at, how plankton biology/ecology was represented, inclusion (or not) of additional dissolved Fe sources to the ocean, plus the parameterization of ocean interior Fe cycle processes (Tagliabue et al., 2016). No model performed particularly ‘well’ against dissolved Fe observations, with a few even exhibiting a negative correlation coefficient globally. The relative performance of cGENIE was amongst the best in terms of correlation coefficient (and model bias) for dissolved iron concentrations at the surface and in the shallow sub-surface, but performed increasingly poorly at greater depth, with a negative correlation coefficient in the 2000-5000 m depth range. One reason for this is because models and data in Tagliabue et al. (2016) were re-gridded to the same high-resolution grid. Because cGENIE is generally configured on a relatively low-resolution grid, significant observed variability occurs on a sub-grid scale, particularly associated with continental margins and hydrothermal ridges. Model-data statistics will thus inherently always tend to be poor, even should large-scale patterns (and hence supply to the surface) of iron in the model be reasonably reproduced. We therefore provide a more detailed model-data comparison here, for each of the 6 dust fields as well as that of Mahowald et al. (2006), with the dissolved Fe observations used by Tagliabue et al. (2016) re-gridded to the cGENIE grid. (Additionally, we filter out extreme dissolved iron concentration values greater than 2 nM, likely associated with unrepresented environments very close to the sediment surface or hydrothermal vents.)

For the ocean surface (the upper 80 m in the cGENIE ocean model grid), the FeMIP dust configuration exhibits a correlation coefficient against the data (re-gridded to the cGENIE grid) of 0.56, compared to 0.43 in Tagliabue et al. (2016). This difference likely principally reflects the differences in the data re-gridding assumptions. The respective correlation coefficients against observed dissolved Fe concentrations in the surface ocean, for each of the 6 dust fields used in this study, are shown in Figure S3, with the Albani dust field leading to the best surface ocean correlation coefficient (0.58), and MIROC-ESM the worst (0.45). That multiple dust fields lead to fit statistics being little worse (or even better) than FeMIP, is reassuring, as the parameter set (mean global (flux-weighted) iron solubility in dust, scaling for the rate of dissolved Fe scavenging onto sinking POM) were tuned for the Mahowald et al. (2006) dust field. For the ocean as a whole (not shown), the correlation coefficients show a relatively similar but lower range (0.37-0.46), with the Albani dust field again leading to the 'best' fit. Perhaps surprisingly, the poorest performing model configuration on a global scale against this data set, is FeMIP.

The conclusion of this analysis is that the substitution of different dust fields into the Mahowald et al. (2006) based configuration of cGENIE used in Tagliabue et al. (2016), does not lead to radically different distributions of dissolved iron in the surface ocean and hence fits to the data, and on a global scale, all lead to an improved correlation coefficient. The surface ocean dissolved iron fields resulting from the 6 alternative dust fields are statistically close to the original configuration (FeMIP) for Albani and Lambert, and to some extent MRI-CGCM3. A notably poorer model-data fit is exhibited in response to the Takemura, MIROC-ESM, and Ohgaito dust fields. However, it is not obvious that these ocean surface spatial-statistical differences translate into any bias in the atmospheric CO_2 response to changing dust flux. For instance, for each of the 4 dust regions, the CO_2 response of Albani

130   vs. Ohgaito is always relatively similar (main text, Figure 4), despite the almost opposite correlation
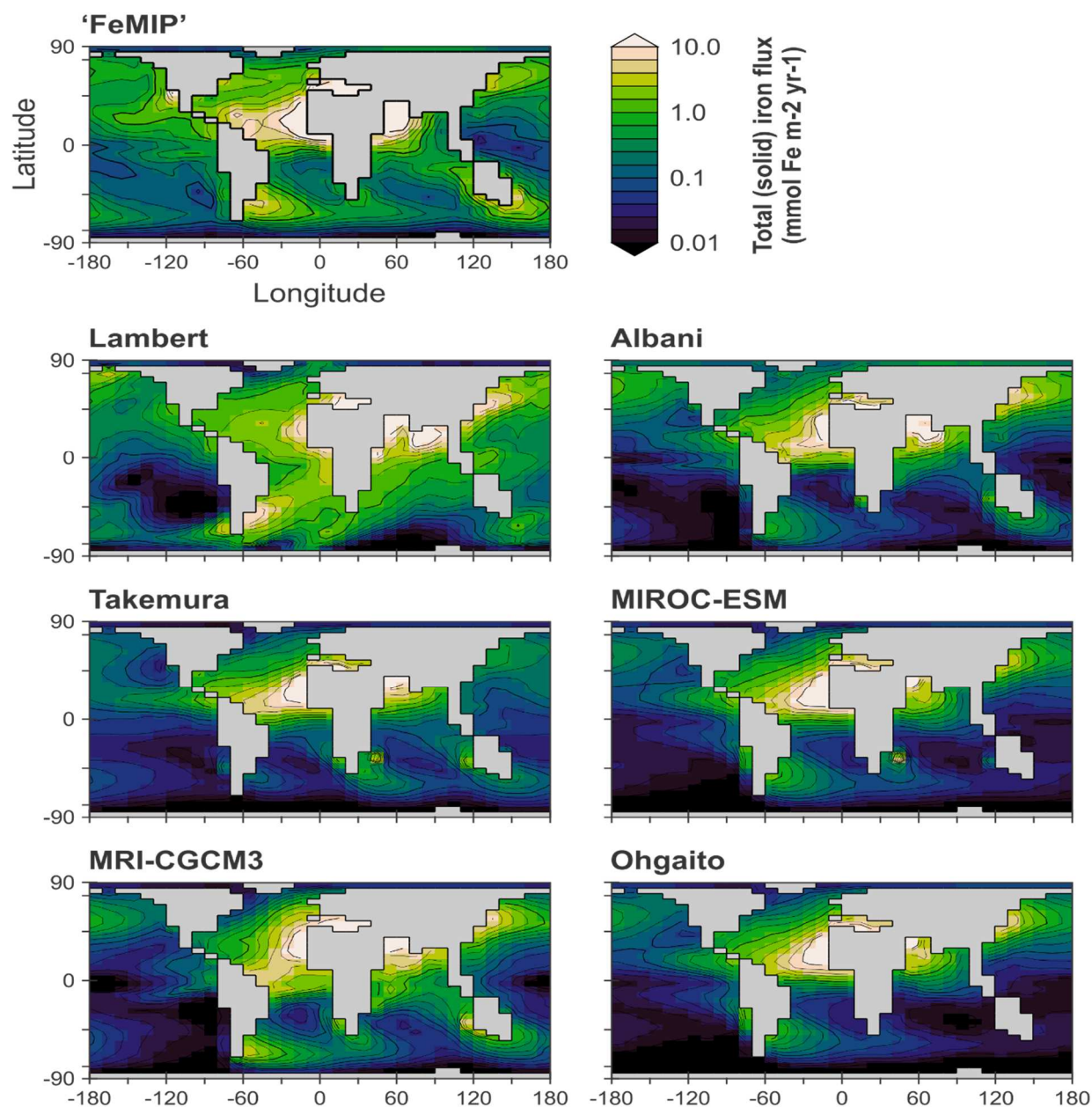
coefficient performance.

Figure S1: The global annual mean distribution of solid iron flux (the iron fraction of dust) applied to the surface ocean in the cGENIE model, for each of the Holocene member of each of the 6 Holocene/LGM dust reconstructions considered in this paper, plus the preindustrial solid iron field of Mahowald et al. (2006) as employed in the cGENIE configuration used in Tagliabue et al. (2016).
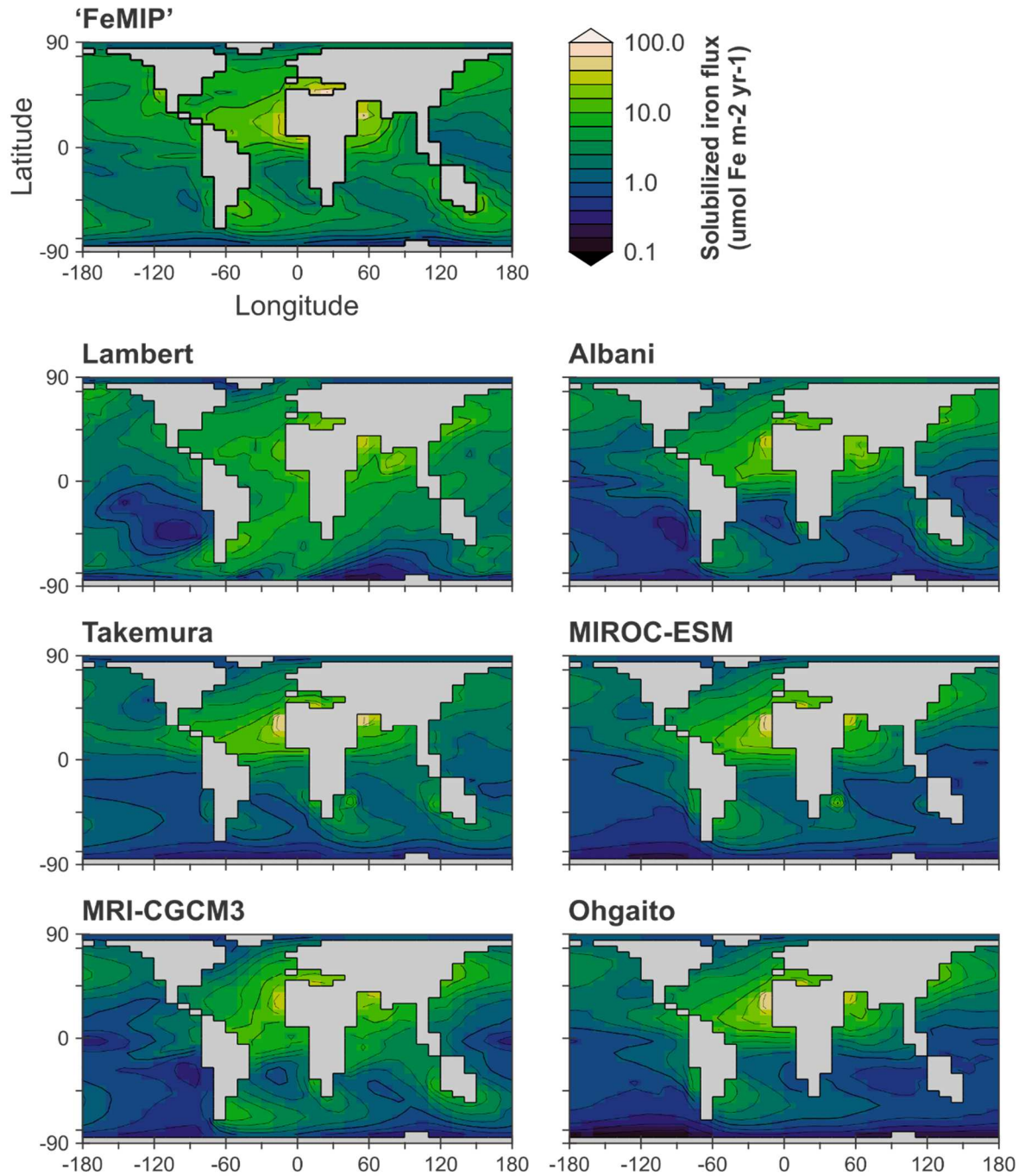
Figure S2: The global annual mean distribution of dissolved iron input flux to the ocean surface layer of the cGENIE model, for each of the Holocene member of each of the 6 Holocene/LGM dust reconstructions considered in this paper, plus the preindustrial dust field of Mahowald et al. (2006). This is linked to the dust distribution shown in Figure S1 via Equation S1.
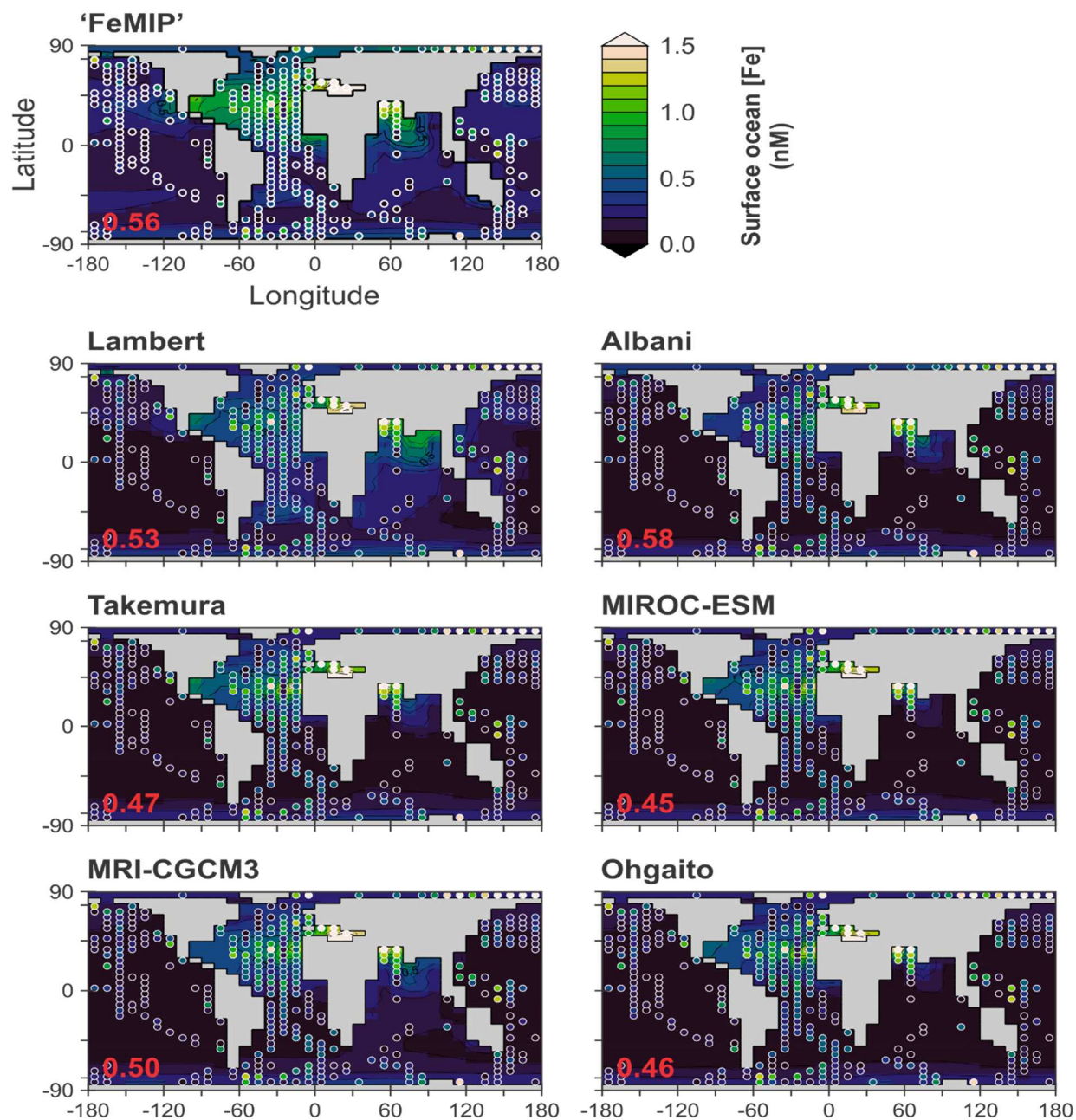
135

Figure S3: Annual mean concentration of dissolved iron in ocean surface layer of the cGENIE model, for each of the Holocene member of each of the 6 Holocene/LGM dust reconstructions considered in this paper, plus the preindustrial dust field of Mahowald et al. (2006). Also shown are the corresponding observed dissolved iron concentrations (from Tagliabue et al. (2016), but excluding values > 2 nM) within the upper 80 m of the water column, and re-gridded (averaged) to the cGENIE ocean model grid. The correlation coefficient between data and model grid cells for which a corresponding observed value exists, are shown in the bottom left of each panel.
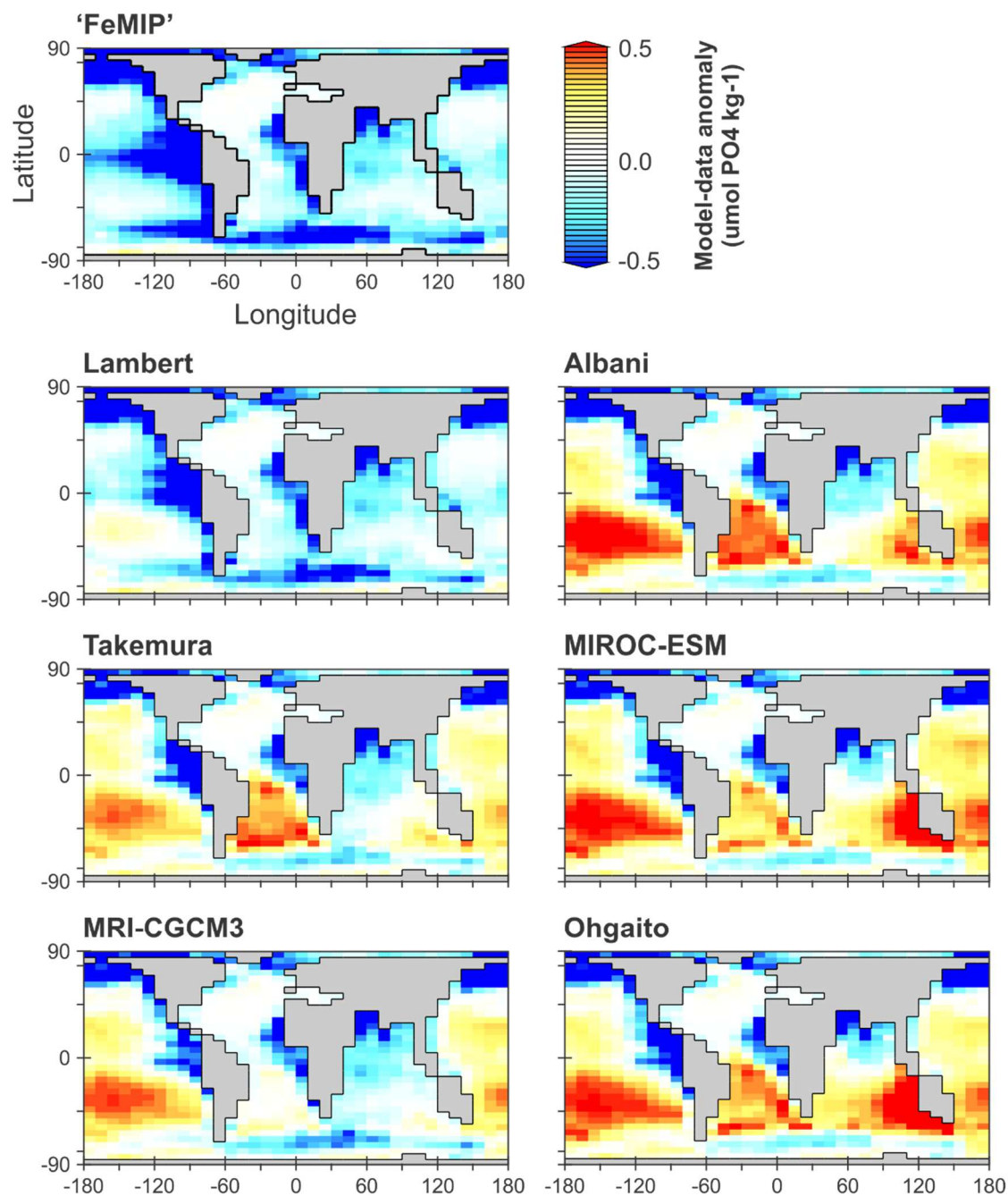
Figure S4: Annual mean concentration of dissolved phosphate in ocean surface layer of the cGENIE model minus climatological observations (annual mean, re-gridded to the cGENIE ocean model grid) (Garcia et al., 2018).

pCO₂ : Dust Relationship

For each simulation we summed up the total amount of dust deposited over the considered region and put these in relationship with the atmospheric CO_2 value for that simulation. The results are shown in Figure S5.
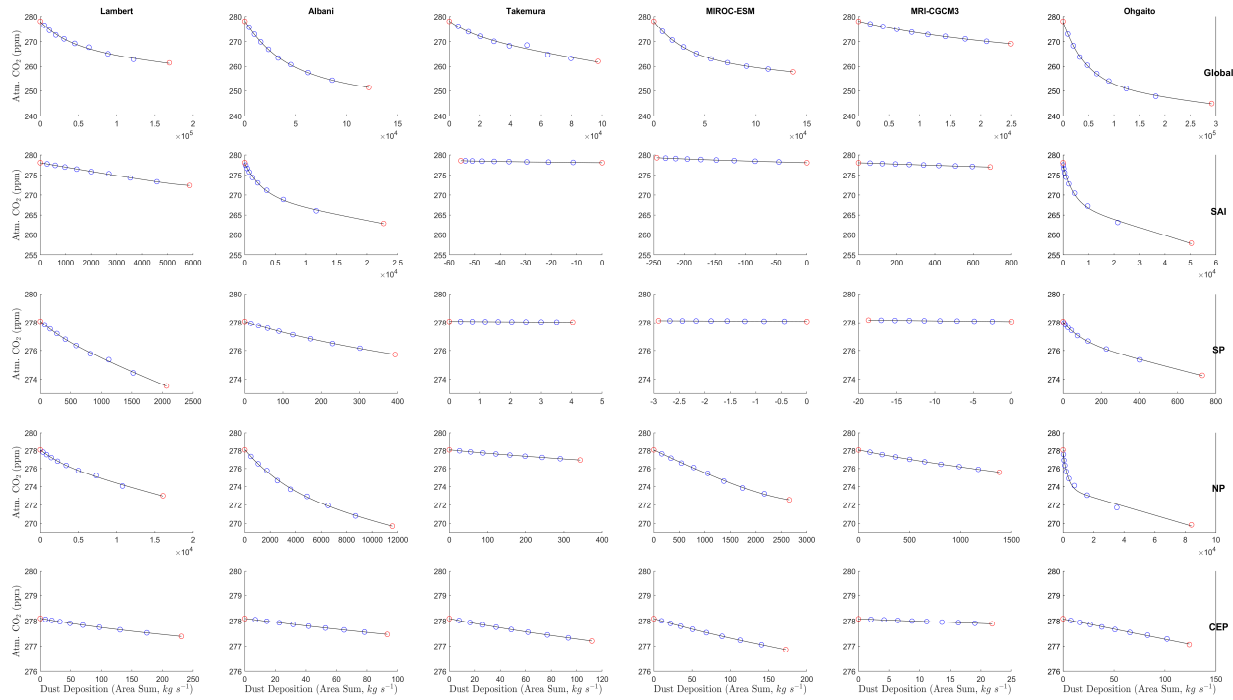
Figure S5: Atmospheric CO_2 levels for each simulation. The x-axis shows the progressive increase of dust deposition (flux summed over each region's area) compared to the Holocene level until LGM levels (both Holocene and LGM levels are distinguished as red circles). The black line is an exponential fit: pCO2 = a*exp(b*Dust)+c*exp(d*Dust)

Temporal Evolution during the Termination

In each HNLC region (Figure 1, main text) we have selected the record that we think is the most

155   representative for the temporal evolution of aeolian dust deposition in that region. These records are
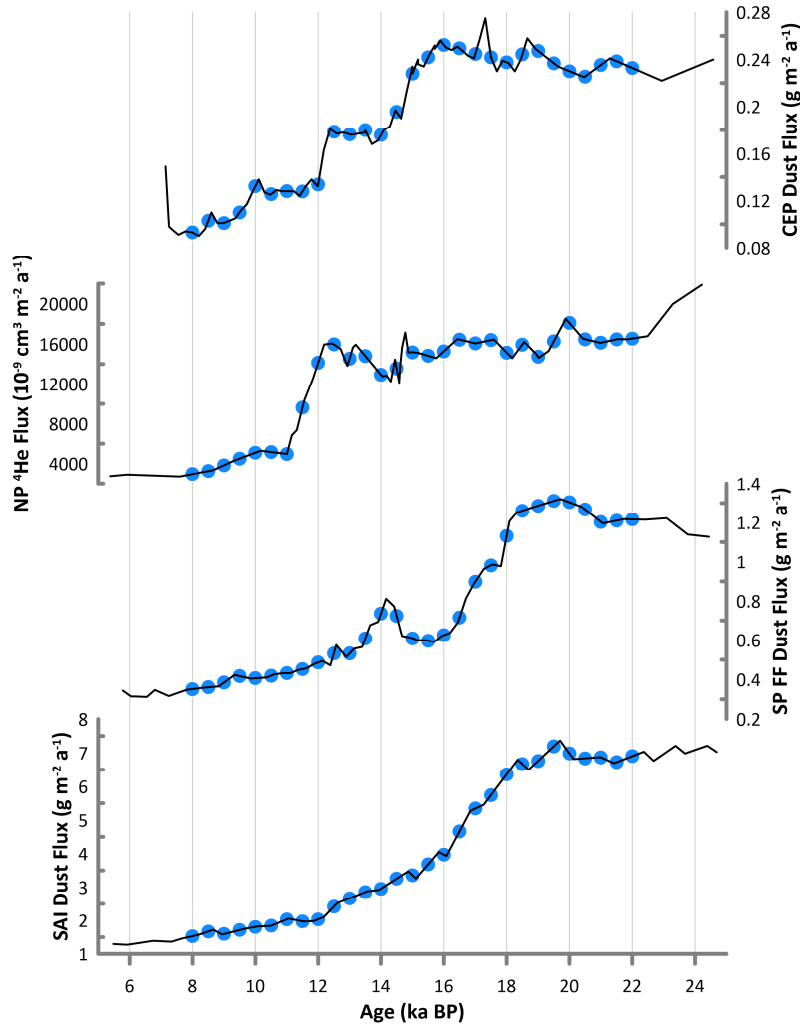
shown in Figure S6.

Figure S6: Time series of aeolian dust fluxes or proxy thereof from marine sediment cores in each HNLC region. The black line shows the data at original resolution, while the blue dots are the resampled values at 500yr resolution.

Sensitivity Analysis

In each HNLC region we have selected the record that we think is the most representative for the

160 temporal evolution of dust deposition variability in that region. Here we show that our results are not

significantly changed by our choice of dust record. In Figure S7 we compare our results from Figure 5

(main text) that use a dust record from the South Atlantic (Anderson et al., 2014) with a different

record from core ODP1090 located closer to Africa (Martínez-Garcia et al., 2011). The region's effect

on atmospheric CO_2 through the whole termination are 10.1 ppmv and 9.3 ppmv for the Anderson and

165 Martinez-Garcia records, respectively (median of the four non-discarded results). The main difference

appears to be during the first CO_2 pulse, with atmospheric CO_2 rising 2.1 ppmv and 3.4 ppmv for the

Anderson and Martinez-Garcia records, respectively . In contrast, CO_2 rose by 1.9 and 1 ppmv

respectively during the second pulse. During the first half of the termination (from LGM to 15 kaBP),

atmospheric CO_2 levels rose by 4.2 and 5.4 ppmv using the Anderson and Martimez-Garcia records,

170 respectively. In the second half they rose by 5.9 and 3.9 ppmv, respectively. The higher dust response

during the early termination in the Martinez-Garcia dust record may be due to influence from the South

African dust source (Albani et al., 2014) that would have declined very rapidly at the beginning of the

termination for the same reasons than the Oceanian source (see main text). Although the final numbers

would change slightly, our conclusion that about 1/3 of the total aeolian iron fertilization effect occurs

175 in the first half, and 2/3 during the second half of the termination would not be altered.
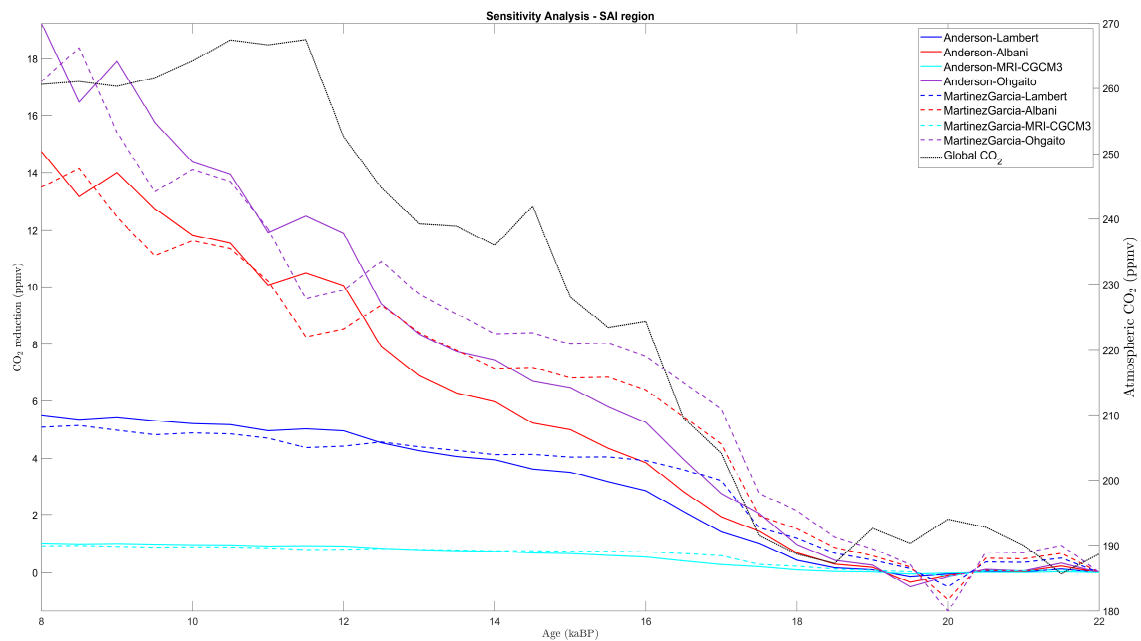
Figure S7: Comparison of the CO₂ reduction using the same fit parameters as in Figure 5 of the main text for two different dust flux marine sediment records from the South Atlantic.

References

Albani, S., Mahowald, N.M., Perry, A.T., Scanza, R.A., Zender, C.S., Heavens, N.G., Maggi, V., Kok, J.F., Otto-
185   Bliesner, B.L., 2014. Improved dust representation in the Community Atmosphere Model. J. Adv. Model.
      Earth Syst. 6, 541–570. https://doi.org/10.1002/2013MS000279

Anderson, R.F., Barker, S., Fleisher, M., Gersonde, R., Goldstein, S.L., Kuhn, G., Mortyn, P.G., Pahnke, K., Sachs,
      J.P., 2014. Biological response to millennial variability of dust and nutrient supply in the Subantarctic
      South Atlantic Ocean. Philos. Trans. R. Soc. A Math. Phys. Eng. Sci. 372.
190   https://doi.org/10.1098/rsta.2013.0054

Baker, A.R., Jickells, T.D., Witt, M., Linge, K.L., 2006. Trends in the solubility of iron, aluminium, manganese and
      phosphorus in aerosol collected over the Atlantic Ocean. Mar. Chem. 98, 43–58.
      https://doi.org/10.1016/J.MARCHEM.2005.06.004

Cao, L., Eby, M., Ridgwell, A., Caldeira, K., Archer, D., Ishida, A., Joos, F., Matsumoto, K., Mikolajewicz, U.,
195   Mouchet, A., Orr, J.C., Plattner, G.-K., Schlitzer, R., Tokos, K., Totterdell, I., Tschumi, T., Yamanaka, Y.,
      Yool, A., 2009. The role of ocean transport in the uptake of anthropogenic CO2. Biogeosciences 6, 375–
      390. https://doi.org/10.5194/bg-6-375-2009

Doney, S.C., Lindsay, K., Fung, I., John, J., 2006. Natural variability in a stable, 1000-yr global coupled climate-
      carbon cycle simulation. J. Clim. 19, 3033–3054. https://doi.org/10.1175/JCLI3783.1

200 Fung, I.Y., Meyn, S.K., Tegen, I., Doney, S.C., John, J.G., Bishop, J.K.B., 2000. Iron supply and demand in the
      upper ocean. Global Biogeochem. Cycles 14, 281–295. https://doi.org/10.1029/1999gb900059

Garcia, H.E., Weathers, K., Paver, C.R., Smolyar, I., Boyer, T.P., Locarnini, R.A., Zweng, M.M., Mishonov, A. V.,
      Baranova, O.K., Seidov, D., Reagan, J.R., 2018. World Ocean Atlas 2018, Volume 4: Dissolved Inorganic
      Nutrients (phosphate, nitrate and nitrate+nitrite, silicate), A. Mishono. ed. NOAA Atlas NESDIS 84.

205 Hülse, D., Arndt, S., Daines, S., Regnier, P., Ridgwell, A., 2018. OMEN-SED 1.0: A novel, numerically efficient
      organic matter sediment diagenesis module for coupling to Earth system models. Geosci. Model Dev. 11,
      2649–2689. https://doi.org/10.5194/gmd-11-2649-2018

Mahowald, N.M., Muhs, D.R., Levis, S., Rasch, P.J., Yoshioka, M., Zender, C.S., Luo, C., 2006. Change in
      atmospheric mineral aerosols in response to climate: Last glacial period, preindustrial, modern, and
210   doubled carbon dioxide climates. J. Geophys. Res. 111. https://doi.org/10.1029/2005JD006653

Martínez-Garcia, A., Rosell-Melé, A., Jaccard, S.L., Geibert, W., Sigman, D.M., Haug, G.H., 2011. Southern
      Ocean dust–climate coupling over the past four million years. Nature 476, 312–315.
      https://doi.org/10.1038/nature10310

Moore, J.K., Braucher, O., 2008. Sedimentary and mineral dust sources of dissolved iron to the world ocean.
215   Biogeosciences 5, 631–656. https://doi.org/10.5194/bg-5-631-2008

Ödalen, M., Nycander, J., Ridgwell, A., Oliver, K.I.C., Peterson, C.D., Nilsson, J., 2020. Variable C∕P composition
      of organic production and its effect on ocean carbon storage in glacial-like model simulations.
      Biogeosciences 17, 2219–2244. https://doi.org/10.5194/bg-17-2219-2020

Parekh, P., Follows, M.J., Boyle, E., 2004. Modeling the global ocean iron cycle. Global Biogeochem. Cycles 18.
220   https://doi.org/10.1029/2003gb002061

Parekh, P., Follows, M.J., Boyle, E.A., 2005. Decoupling of iron and phosphate in the global ocean. Global Biogeochem. Cycles 19, 1–16. https://doi.org/10.1029/2004GB002280

Ridgwell, A.J., 2001. Glacial-interglacial perturbations in the global carbon cycle. University of East Anglia.

Tagliabue, A., Aumont, O., DeAth, R., Dunne, J.P., Dutkiewicz, S., Galbraith, E., Misumi, K., Moore, J.K., Ridgwell, A., Sherman, E., Stock, C., Vichi, M., Völker, C., Yool, A., 2016. How well do global ocean biogeochemistry models simulate dissolved iron distributions? Global Biogeochem. Cycles 30, 149–174. https://doi.org/10.1002/2015GB005289

Tagliabue, A., Bopp, L., Roche, D.M., Bouttes, N., Dutay, J.-C., Alkama, R., Kageyama, M., Michel, E., Paillard, D., 2009. Quantifying the roles of ocean circulation and biogeochemistry in governing ocean carbon-13 and atmospheric carbon dioxide at the last glacial maximum. Clim. Past 5, 695–706. https://doi.org/10.5194/cp-5-695-2009